Atmos. Meas. Tech. Discuss., https://doi.org/10.5194/amt-2018-278
Manuscript under review for journal Atmos. Meas. Tech.
Discussion started: 9 November 2018

Atmospheric Measurement Techniques Discussions

Simulating precipitation radar observations from a geostationary satellite

By

Atsushi Okazaki[1], Takumi Honda[1], Shunji Kotsuki[1,2],
Moeka Yamaji[3], Takuji Kubota[3], Riko Oki[3],
Toshio Iguchi[4],
and Takemasa Miyoshi[1,2,5,6,7]

[1]RIKEN Center for Computational Science, Kobe, Japan
[2] RIKEN interdisciplinary Theoretical and Mathematical Sciences Program, Kobe, Japan
[3]Earth Observation Research Center, Japan Aerospace Exploration Agency, Tsukuba, Japan
[4]National Institute of Information and Communications Technology, Koganei, Japan
[5]Department of Atmospheric and Oceanic Science, University of Maryland, College Park, College Park, Maryland
[6]Japan Agency for Marine-Earth Science and Technology, Yokohama, Japan
[7]Prediction Science Laboratory, RIKEN Cluster for Pioneering Research, Kobe, Japan

Corresponding authors: Atsushi Okazaki and Takemasa Miyoshi, RIKEN Center for Computational Science, 7-1-26 Minatojima-minami-machi, Chuo-ku, Kobe, Hyogo 650-0047, Japan (atsushi.okazaki@riken.jp, takemasa.miyoshi@riken.jp)

Atmos. Meas. Tech. Discuss., https://doi.org/10.5194/amt-2018-278
Manuscript under review for journal Atmos. Meas. Tech.
Discussion started: 9 November 2018

Atmospheric Measurement Techniques Discussions

Abstract

Spaceborne precipitation radars, such as the Tropical Rainfall Measuring Mission (TRMM) and the Global Precipitation Measurement (GPM) Core Observatory, have been important platforms to provide a direct measurement of three-dimensional precipitation structure globally. Building upon the success of TRMM and GPM Core Observatory, the Japan Aerospace Exploration Agency (JAXA) is currently surveying the feasibility of a potential satellite mission equipped with a precipitation radar on a geostationary orbit. The quasi-continuous observation realized by the geostationary satellite radar would offer a new insight into meteorology and would advance numerical weather prediction (NWP) through their effective use by data assimilation.

Although the radar would be beneficial, the radar on the geostationary orbit measures precipitation obliquely at off-nadir points. Besides, the observing resolution will be several times larger than those onboard TRMM and GPM Core Observatory due to the limited antenna size that we could deliver. The tilted sampling volume and the coarse resolution would result in more contaminations from the surface clutters. To investigate the impact of these limitations and to explore the potential usefulness of the geostationary satellite radar, this study simulates the observation data for a typhoon case using an NWP model and a radar simulator.

The results demonstrate that it would be possible to obtain three-dimensional precipitation data. However, the quality of the observation depends on the beam width, the beam sampling span, and the position of precipitation systems. With a wide beam width and a coarse beam span, the radar cannot observe weak precipitation at low altitudes due to the surface clutters. The limitation can be mitigated by oversampling (i.e., a wide beam width and a fine sampling span). With a narrow beam width and a fine beam sampling span, the surface clutter interference is confined to the surface level. When the precipitation system is located far from the nadir, the precipitation signal is obtained only for strong precipitation.

Atmos. Meas. Tech. Discuss., https://doi.org/10.5194/amt-2018-278
Manuscript under review for journal Atmos. Meas. Tech.
Discussion started: 9 November 2018

Atmospheric Measurement Techniques Discussions

1. Introduction

Knowing the distribution of precipitation in space and time is essential for scientific developments as precipitation plays a key role in global water and energy cycles in the Earth system. Such knowledge is also indispensable to our daily lives and disaster monitoring and prevention. However, observing precipitation globally is not an easy task. Ground-based observations may not adequately represent the rainfall amounts of a broader area since the vast surface of the earth remains unobserved (Kidd et al., 2016). Alternatively, satellites provide an ideal platform to observe precipitation globally. There are three types of methods to observe or estimate precipitation from satellites: visible and infrared, passive microwave, and active microwave (radar). Among them, radar is the most direct method and is the only sensor that can provide three-dimensional structure of precipitation. The first satellite equipped with precipitation radar was the Tropical Rainfall Measuring Mission (TRMM) launched in 1997 (Kummerow et al., 1998; Kozu et al., 2001), and the first satellite-borne dual-frequency precipitation radar onboard the Global Precipitation Measurement (GPM) Core Observatory was launched in 2014 (Hou et al., 2014; Skofronick-Jackson et al., 2017). The observations produced by the precipitation radars onboard the low-earth-orbiting satellites have been contributing to enhance our knowledge on meteorology. For instance, their ability to see through clouds helps understand storm structures (Kelly et al., 2004) and the nature of convection (e.g. Takayabu 2006; Hamada et al., 2015; Houze et al., 2015).

Building upon the success of the TRMM and GPM Core Observatory, the Japan Aerospace Exploration Agency (JAXA) is currently studying the feasibility of a geostationary satellite equipped with precipitation radar (hereafter, simply “GeoSat/PR”). The main advantage of GeoSat/PR over the existing ones with precipitation radar is the observation frequency. Because the previous satellites are low earth orbiters, they cannot observe the same area frequently. For instance, TRMM overpasses a 500 by 500 km^2 box 1-2 times a day on average (Bell et al., 1990). To make the situation worse, it is difficult to capture the whole figure of a large-scale precipitation system (e.g. tropical cyclone) at once

Atmos. Meas. Tech. Discuss., https://doi.org/10.5194/amt-2018-278
Manuscript under review for journal Atmos. Meas. Tech.
Discussion started: 9 November 2018

due to the narrow scan swath (e.g. 245 km for KuPR on GPM Core Observatory). Alternatively, GeoSat/PR stays at the same location all the time and continuously measures precipitation in its range of observation. Those data are expected to help understand important scientific issues. Furthermore, those frequent data could improve the skill of numerical weather prediction (NWP) through data assimilation, leading to more accurate and timely warnings of floods and landslides.

Although GeoSat/PR would be beneficial, it has potential disadvantages. Since GeoSat/PR measures precipitation from the geostationary orbit, it measures precipitation obliquely at off-nadir points. It is unclear how severely this may degrade the observation. In addition, the tilted sampling volume worsens the contamination of the precipitation echo by the surface clutter. Takahashi (2017) showed that the clutter height monotonically increases with the incident angle from the wide swath observation during the end-of-mission experiment of the TRMM. The impact of the surface clutter interference with a large incident angle would be large if the horizontal resolution of the radar is coarse, and that is the case for GeoSat/PR. The horizontal resolution is limited by the antenna size and wavelength. A larger antenna is needed for higher resolution. However, it is challenging to construct a large antenna on a geostationary orbit. Currently we consider a 20-m-by-20-m square antenna as a feasible choice, whose spatial resolution is 20 km at nadir, that is several times larger than that of TRMM/PR (4.3 km). To investigate the mission feasibility of GeoSat/PR, it is important to simulate observation of GeoSat/PR and to find its potential usefulness and weakness.

In the past decade, a geostationary radar instrument known as the Next Generation Weather Radar (NEXRAD) In Space (NIS; Im et al., 2007) has been proposed. A few studies demonstrated the capability of NIS. Lewis et al. (2011) examined the feasibility of a 35 GHz Doppler radar to observe the wind field. They showed that the direct measurement of winds from the geostationary orbit would be possible for a hurricane case. Li et al. (2017) evaluated the impact of surface clutter for the same radar assuming a uniform rain layer. They showed that most of rain echoes at off-nadir scanning angles will not be contaminated by the surface clutter, when rain intensity is greater than 10 mm h^{-1}.

Atmos. Meas. Tech. Discuss., https://doi.org/10.5194/amt-2018-278
Manuscript under review for journal Atmos. Meas. Tech.
Discussion started: 9 November 2018

Atmospheric Measurement Techniques Discussions

107 However, the impact of the surface clutter and the oblique measurement would depend on the shape
108 and position of the precipitation system. This study extends Li et al. (2017) for a realistic case. By
109 considering the importance to societal and scientific benefit, we chose a typhoon as a test case in this
110 study. We investigate the impact with various typhoon locations and radar parameters such as radar
111 beam width and sampling span for realistic scenarios of a simulated typhoon case.

112 This paper is structured as follows. Section 2 describes the proposed specifications of GeoSat/PR
113 and presents the newly-developed radar simulator. Section 3 describes the characteristics of the
114 observation with GeoSat/PR for an idealized case. Section 4 presents the results of applying the radar
115 to a typhoon case. Section 5 provides the sensitivity results to the location of the typhoon. Finally,
116 Section 6 provides conclusions.

117

118 **2. Radar simulator**

119 **2.1. Radar specifications**

120 The specifications of GeoSat/PR are summarized in Table. 1. The GeoSat/PR is anticipated at 13.6
121 GHz, the same as KuPR onboard GPM Core Observatory. We assume a 20-m-by-20-m square phased
122 array radar with the half beam width (-3 dB) of 0.032°, with which we can achieve horizontal resolution
123 of 20 km at the nadir point on the earth surface. The range resolution is 500 m. Though shorter-range
124 resolution is technically viable, we adopt this value by considering the balance to the horizontal
125 resolution. The number of the range bins is 60; the corresponding height of the beam center ranges
126 from the surface to 30 km at nadir. The scan angle is ±6°, which covers a circular disk with a diameter
127 of 8400 km on Earth's surface. If GeoSat/PR were placed at 135°E of the equator, it would cover from
128 Sumatra to New Caledonia, and from Australia to the southern half of Japan.

129 We assume that the satellite can complete the full disk scan within one hour. In addition to the normal
130 mode, it is expected to have several modes and can observe a targeting precipitation system intensively
131 as in Himawari-8 (Bessho et al., 2016). In this study, we focus only on snap-shots and do not consider

Atmos. Meas. Tech. Discuss., https://doi.org/10.5194/amt-2018-278
Manuscript under review for journal Atmos. Meas. Tech.
Discussion started: 9 November 2018

Atmospheric Measurement Techniques Discussions

the time for GeoSat/PR to complete the full disk scan.

2.2. Precipitation reflectivity

This subsection describes how to calculate reflectivity measured by GeoSat/PR (Z_m). First, we convert model hydrometeors to reflectivity on the model grid (Z_e) using an existing software called Joint Simulator for Satellite Sensors (Joint-Simulator; Hashino et al., 2013). The Joint-Simulator is a suite of software that simulates satellite observations based on atmospheric states simulated by cloud-resolving models. The computation of reflectivity in Joint-Simulator is based on Masunaga and Kummerrow (2005) as follows:

$$Z_e = \frac{\lambda^4}{\pi^5 |K|^2} \bar{\sigma}_b, \tag{1}$$

with

$$\bar{\sigma}_b = \sum_{i=1}^{5} \int_0^{\infty} \sigma_{b,i}^s(D) N(D) dD, \tag{2}$$

where λ is the wavelength, K the function of the complex reflractivity index of scattering particles, and $\bar{\sigma}_b$ the total backscattering coefficient per unit volume. Following Masunaga and Kummerow (2005), $|K|^2$ is assumed to be a constant (0.925) in this study. The total backscattering coefficients are obtained by summing single-particle backscattering (σ_b^s) for the *i* th hydrometeor specie following its drop size (D) distribution ($N(D)$). In this study, up to five hydrometeor species were considered. The Mie approximation is assumed to calculate the single-particle backscattering for all species (Masunaga and Kummerow, 2005).

After calculating the reflectivity on the model grid, they are integrated over the scattering volume following the antenna pattern. The radar-received power from precipitation (P_r) of the beam pointing range r_0 and scan angle θ_0 and ϕ_0 is given by

$$P_r = \frac{P_t \lambda^2}{(4\pi)^3} \int_{r_0 - c\tau/4}^{r_0 + c\tau/4} \int_{\theta_0 - \pi}^{\theta_0 + \pi} \int_{\phi_0 - \pi/2}^{\phi_0 + \pi/2} f^4(\theta, \phi) r^{-2} Z_e(r, \theta, \phi) \cos\theta \, d\phi \, d\theta \, dr, \tag{3}$$

where P_t is the transmitted power, c the speed of light, τ the pulse duration, and f^4 the two-way

Atmos. Meas. Tech. Discuss., https://doi.org/10.5194/amt-2018-278
Manuscript under review for journal Atmos. Meas. Tech.
Discussion started: 9 November 2018

Atmospheric Measurement Techniques Discussions

effective beam weighting function. Here we assumed the antenna pattern as the Gaussian function, which is approximated by the following fifth-order polynomial (Fig. 1; Gaspari and Cohn, 1999):

$$f^2(\psi) = \begin{cases} -\frac{1}{4}\psi^5 + \frac{1}{2}\psi^4 + \frac{5}{8}\psi^3 - \frac{5}{3}\psi^2 + 1 & (0 \le \psi < 1) \\ \frac{1}{12}\psi^5 - \frac{1}{2}\psi^4 + \frac{5}{8}\psi^3 + \frac{5}{3}\psi^2 - 5\psi + 4 - \frac{2}{3}\psi^{-1} & (1 \le \psi < 2) \\ 0 & (2 \le \psi) \end{cases} \quad (4)$$

where $\psi = \sqrt{(\theta - \theta_0)^2 + (\phi - \phi_0)^2}/\Psi$, and Ψ is obtained by solving the equation $f\left(\frac{\theta_B}{2}/\Psi\right) = 0.5$ for Ψ. The radar reflectivity measured by GeoSat/PR is calculated as follows:

$$Z_m = \frac{\int_{r_0-\frac{c\tau}{4}}^{r_0+\frac{c\tau}{4}} \int_{\theta_0-\pi}^{\theta_0+\pi} \int_{\phi_0-\frac{\pi}{2}}^{\phi_0+\frac{\pi}{2}} f^4(\theta,\phi) r^{-2} Z_e(r,\theta,\phi)\, cos\theta\, d\phi\, d\theta\, dr}{\int_{r_0-\frac{c\tau}{4}}^{r_0+\frac{c\tau}{4}} \int_{\theta_0-\pi}^{\theta_0+\pi} \int_{\phi_0-\frac{\pi}{2}}^{\phi_0+\frac{\pi}{2}} f^4(\theta,\phi) r^{-2}\, cos\theta\, d\phi\, d\theta\, dr}. \quad (5)$$

2.3. Surface clutter

Surface clutter echoes contaminate the precipitation signals. In this study, we assumed that the surface is completely covered by the ocean for simplicity. Radar-received power from the sea surface (P_s) was calculated by

$$P_s = \frac{P_t \lambda^2}{(4\pi)^3} \iint_A \frac{f^4(\theta,\phi)\sigma_0}{r^4} dA \quad (6)$$

where σ_0 is the normalized radar cross section (NRCS) of the ocean surface, and A the scattering area. We obtained σ_0 using a model proposed by Wentz et al. (1984) based on observations from a microwave scatterometer onboard the Seasat satellite. The model expresses σ_0 as,

$$\sigma_0 = b_0 (U_{10})^{b_1} \quad (7)$$

where U_{10} is the 10-m wind speed, and b_0 and b_1 are fitted parameters. The NRCS for various wind speed is shown in Fig. 2.

3. Homogeneous case

To understand the characteristics of the radar observation, we first show the results from an idealized

Atmos. Meas. Tech. Discuss., https://doi.org/10.5194/amt-2018-278
Manuscript under review for journal Atmos. Meas. Tech.
Discussion started: 9 November 2018

Atmospheric Measurement Techniques Discussions

case, in which we assume the atmosphere below 2 km is uniformly filled with a certain amount of hydrometeor. We tested five cases: 20, 30, 40, 50, and 60 dBZ. The corresponding precipitation intensity is roughly 1, 2, 5, 20, and 60 mm h^{-1} if the hydrometeor consists of only rain. The 10-m wind speed was fixed at 10 m s^{-1} uniformly for all cases. The horizontal resolution of the radar was assumed to be 20 km at the nadir point.

Figure 3a shows P_r for the case of 60 dBZ. Two features are apparent in the figure. The first is that the precipitation signal is beyond the precipitation area and becomes taller along with the distance from the nadir, and the second is that P_r decreases monotonically with height. Here and hereafter, the distance was measured along the earth surface.

Before discussing the reason for these, first we explain the scattering volume of the GeoSat/PR. Here, the scattering volume of the beam pointing range r_0 and scan angle θ_0 and ϕ_0 is defined as the area where r, θ, and ϕ satisfy both $r_0 - \frac{c\tau}{4} \le r \le r_0 + \frac{c\tau}{4}$ and $f^2(\psi) > 0$. Figure 4 shows a schematic image of the scattering volume. At the nadir, the incident angle is zero, and the scattering volume is nearly parallel to the earth surface (Fig. 4a). As the incident angle increases, the scattering volume becomes tilted against the earth surface (Fig. 4b). As a result, the upper edge of the scattering volume reaches as high as 20 km when the beam center of the GeoSat/PR is at a point 4000 km away from the nadir even in the lowest range bin (range bin number 1 in Fig. 5b). In the same angle but the highest range bin, the scattering volume ranges from 2 km to 44 km in height (range bin number 60 in Fig. 5b).

When the beam center is at the level higher than the precipitating area, there is no precipitation around the beam center. On the other hand, the tip of the scattering volume may touch the precipitating area with the tilted scattering volume at off-nadir. In such a case, the scattering volume is not fully filled with precipitation. Such nonuniform beam filling (NUBF) results in the reduction of P_r with $Z_e = 0$ in the upper part of the volume compared with the fully filled case. Although the value is small, still GeoSat/PR catches the signal of precipitation, and thus P_r has a value even when the beam center

Atmos. Meas. Tech. Discuss., https://doi.org/10.5194/amt-2018-278
Manuscript under review for journal Atmos. Meas. Tech.
Discussion started: 9 November 2018

Atmospheric Measurement Techniques Discussions

is at the point higher than the precipitating area. As the scattering volume becomes more tilted against the earth surface along with the distance from the nadir (Fig. 5a), the maximum height at which the beam gets a signal from precipitation becomes higher along with the distance from the nadir. Hence, we have the signal beyond the precipitation area and the area becomes taller along with the distance from the nadir.

The P_r magnitude dependence on the height is also explained by the NUBF. Due to the experimental setting where precipitation exists only in the atmosphere below 2 km, the beam with the scattering volume touching the level higher than 2 km are not fully filled with precipitation. The higher the GeoSat/PR observes, the less the scattering volume is filled with precipitation. Accordingly, P_r decreases with height.

The pattern of P_s is similar to that of P_r, showing dependence on the distance from the nadir (Fig. 3b) because σ_0 is a function of the incident angle (Fig. 2).

Figure 6 shows signal-to-clutter ratio (SCR) defined as P_r/P_s (dB). The larger SCR, the less contaminated by the clutter. In the figure, areas where the reflectivity from precipitation exceeds 0 dBZ are shaded. For all the cases, SCR is the largest at nadir and high altitudes. The minimum SCR is found at the surface level around 500 km away from the nadir reflecting the peak of the echo from the surface clutter. As expected, SCR becomes large when precipitation is strong since the received power from the precipitation becomes larger while P_s is the same for all the cases. The GeoSat/PR can perceive precipitation only at the nadir point in the case of 20 dBZ (Fig. 6a), but SCR is larger than zero over the whole precipitating area in the case of 60 dBZ (Fig. 6e) except for the surface level in 0 to 1000 km away from the nadir. The comparison of the two cases also suggests that the surface clutter contaminates the precipitation signal from high altitudes for weak precipitation. On the other hand, if the precipitation is strong enough, the clutter interference is very limited, and we should get the signal even at the surface level.

The simulated results are consistent with Takahashi (2017) and Li et al. (2017), suggesting that both

220 results be plausible.

221

222 **4. Typhoon case**

223 Section 3 presented the characteristics of reflectivity of GeoSat/PR. However, what we can observe
224 will depend on the size and structure of the target precipitation system. To investigate the capability of
225 GeoSat/PR in detail, we ran an atmospheric model and applied the radar simulator to produce synthetic
226 observations of reflectivity. As an example, we chose Typhoon Soudelor in 2015, which was the
227 strongest typhoon in that year. Soudelor, generated on 1 August 2015 around Marshall Islands, rapidly
228 intensified to Super Typhoon equivalent to Category 5 Hurricane within 24 hours from the generation
229 and dissipated on 11 August 2015. In this study, we focused on the mature stage of Soudelor at 0000
230 UTC 5 August 2015.

231 In this section, we focus on the sensitivity to two radar parameters: beam width and beam sampling
232 span. Three cases were examined: the first adopts the beam width and sampling span of 20 km, the
233 experiment named "bw20bs20." The second uses the 5-km beam width and span (bw05bs05), and the
234 third uses 20-km resolution of beam width, but the beam span is chosen to be 5 km (bw20bs05),
235 representing an over-sampling case. The settings are summarized in Table 2.

236

237 **4.1. SCALE-RM simulation**

238 We used a regional cloud-resolving model, SCALE-RM version 5.0.0 (Nishizawa et al., 2015; Sato
239 et al., 2015) to simulate Soudelor. SCALE-RM is based on the SCALE library for weather and climate
240 simulations. The source code and documents of the SCALE library including SCALE-RM are publicly
241 available at http://r-ccs-climate.riken.jp/scale/. The moist physical process is parameterized by a 6-
242 class single-moment bulk microphysics scheme (Tomita et al., 2008), and the five species of
243 hydrometeors (rain, cloud water, cloud ice, snow, and graupel) were used to calculate the radar
244 reflectivity. We use the level-2.5 closure of the Mellor–Yamada–Nakanishi–Niino turbulence scheme

Atmos. Meas. Tech. Discuss., https://doi.org/10.5194/amt-2018-278
Manuscript under review for journal Atmos. Meas. Tech.
Discussion started: 9 November 2018

Atmospheric Measurement Techniques Discussions

to represent subgrid-scale turbulences (Nakanishi and Niino 2004). For shortwave and longwave radiation processes, the Model Simulation Radiation Transfer code (MSTRN) X (Sekiguchi and Nakajima, 2008) is used. See http://r-ccs-climate.riken.jp/scale/ for more detail.

We performed an offline nesting simulation. The horizontal grid spacings and the number of vertical levels for the outer (inner) domain were 15 km (3 km) and 36 levels (56 levels), respectively. Hereafter, the simulation for the outer (inner) domain is referred to as D1 (D2) (Fig. 7a). The initial and lateral boundary conditions for D1 were taken from the National Centers for Environmental Prediction (NCEP) Global Forecasting System (GFS) operational analyses at 0.5° resolution every 6 hour. The initial and lateral boundary conditions for D2 were taken from D1. The simulation covers the period from 0000 UTC 28 July 2015 (0000 UTC 28 July 2015) to 0000 UTC 9 August 2015 (0000 UTC 7 August 2015) for D1 (D2).

Figure 7 shows the Soudelor's track and minimum sea level pressure (MSLP) at the typhoon center from the best track of the Japan Meteorological Agency (JMA) and the D1 and D2 simulations. The JMA best track shows a rapid decrease of MSLP during the three days from 1 August. D1 captures the rapid intensification while D2 shows a slightly slower intensification than the best track. As for the track, both D1 and D2 closely follow the best track albeit slightly shifted northward. We used D2 as a reference to simulate radar observations.

4.2. Results

Figures 8 and 9 show radar reflectivity near the surface level and its vertical cross section in a mature stage of the simulated Soudelor (0000 UTC 5 August 2015). The results are shown in the longitude-latitude coordinate for Fig. 8 (a) and in the scan-angle coordinate of the GeoSat/PR for Fig. 8 (b-d) covering the same domain as Fig. 8 (a). As in the homogeneous case, areas where the reflectivity from precipitation exceeds 0 dBZ are shaded by grey.

Figure 8 (a) and 9 (a) show the reflectivity of the full-resolution nature run for reference. The figures

Atmos. Meas. Tech. Discuss., https://doi.org/10.5194/amt-2018-278
Manuscript under review for journal Atmos. Meas. Tech.
Discussion started: 9 November 2018


Atmospheric Measurement Techniques Discussions

show the typical structure of a tropical cyclone characterized by no rainfall within the eye, heavy rainfall in the eye wall, and the spiral outer-rainband structure.

The bw20bs20 captures the spatial distribution well but without fine structures. The difference is noticeable in the outer rainband (gray-colored area) in which the shape of the bands is different from the reference. With the tilted and relatively large scattering volume, the radar catches the signal of precipitation that is in the level higher than the level shown in the figure. The bw20bs20 also misses the local maxima of precipitation. For instance, the strongest precipitation south of the eye (red area in Fig. 8a) was not well captured by bw20bs20. This is because the echo from sharp and strong precipitation was averaged out due to NUBF within the relatively large scattering volume. For the vertical cross-section, the observation roughly captures the structure albeit in a jaggy and discretized manner because of the tilted and relatively large scattering volume (Fig. 9b). The tilted scattering volume also results in the precipitation echo taller than the reference as discussed in Sect. 3.

On the other hand, the satellite observes precipitation accurately for both spatial and vertical cross-sections in bw05bs05 (Fig. 8d and Fig. 9d).

In the case of bw20bs05 (i.e. oversampling case), the radar inherited the shortcomings in bw20bs20 due to the wide beam width: the larger precipitated area in the outer rainband (Fig. 8c) and taller precipitation pattern (Fig. 9c) compared with the reference. On the other hand, the results were arguably improved thanks to the fine sampling span compared with bw20bs20. For instance, the strong precipitation south of the eye was well captured compared with bw20bs20 (Fig. 9c). Furthermore, individual convective cells south of the typhoon were observed as individual cells although they were blurred due to NUBF within the large scattering volume. This is because the finer sampling span increased the probability for the beam center to hit the area of heavy rainfall.

To compare the skills quantitatively, we computed the threat scores with a threshold of 20, 30, 40, and 50 dBZ for all the experiments. Figure 10 shows that bw05bs05 is the best and also shows the benefit of oversampling. Namely, the score of bw20bs05 increased by more than 20 % on average for

Atmos. Meas. Tech. Discuss., https://doi.org/10.5194/amt-2018-278
Manuscript under review for journal Atmos. Meas. Tech.
Discussion started: 9 November 2018

all the thresholds compared with that of bw20bs20.

Figures 9 and 10 also shows the impact of the surface clutter. The hatched area in Fig. 9 shows the area where SCR is less than or equal to zero. Assuming that the SCR of zero is the minimum threshold to indicate whether the clutter interference will be serious (Li et al., 2017), the hatched area is considered as unobservable. The unobservable area was confined up to 3-km in bw05bs05, while they reached as high as 7 km in bw20bs20 and bw20bs05. Thus, to reduce the impact of the surface clutter, the beam width needs to be narrow enough.

5. Dependence on the position of typhoon

At other than the nadir point, the radar observes precipitation obliquely and consequently the precipitation echo is easy to be contaminated by the surface clutter. As mentioned in Sect. 3, how severely surface clutter contaminates the precipitation echo depends on the incident angle of the beam, which corresponds to the distance from the nadir. Therefore, the location of the target precipitation system should have an impact on the quality of the observations. This section investigates the sensitivity to the location of the typhoon.

We used the simulated Typhoon Soudelor as the reference as in Sect. 4. We picked out the mature stage of the typhoon whose center is in 18° N, 136° E as an example and moved it north and south to represent typhoons whose center is in 10° N, 20° N, and 30° N. We assumed the longitudinal position of the typhoon centers were the same as the sub-satellite point for all the cases to compare the difference originating from the latitudinal position of the typhoon center. The radar used in this section was the same as the one in the bw20bs05.

Figure 11 shows the precipitation echo at the near surface level for the three cases together with the reference. Among them, the precipitation pattern in 10° N was the most similar to the reference, and the threat score was the highest (Fig. 13). As the typhoon position is away from the sub-satellite point, the precipitation is observed weaker with the outer-rainband area more expanded, and the threat score

Atmos. Meas. Tech. Discuss., https://doi.org/10.5194/amt-2018-278
Manuscript under review for journal Atmos. Meas. Tech.
Discussion started: 9 November 2018

becomes lower (Fig. 13). As discussed in the previous sections, those are due to the widely tilted scattering volume with which the beam captures the signal of precipitation in high altitude whose intensity is weaker than that in the level shown (cf. Fig. 12). The tilted scattering volume also resulted in vertically extended precipitation echo (Fig. 12). The further away from the nadir, the more vertically extended the precipitation echo. This is also true for the clutter height (SCR ≤ 0): the further away from the nadir, the higher the clutter height. However, this is only the case for the area with weak precipitation. In the area with heavy precipitation at a higher latitude, the impact of the surface clutter is limited to the near surface level. For instance, the strongest precipitation in the south of the eye is not affected by the surface clutter at all in the case of 30° N (Fig. 12d), while those are masked by the clutter in the cases of 10° N and 20° N (Fig. 12b and 12c). Those results are also evident in the threat score (dashed line in Fig. 13). The surface clutter is determined by cross section σ_0 integrated over the scattering area A, and both σ_0 and A decrease along with the incident angle in this area. Therefore, the echo from the sea surface clutter becomes smaller and SCR becomes larger along with the latitude.

We obtained the similar results as shown in Sect. 3 with the typhoon case. When the observation target is in low latitude (i.e. close to the nadir), the clutter height is low, and the radar can observe weak precipitation free from clutter at high altitudes. It should be difficult to observe precipitation at the near surface level, even if the precipitation is strong. In case the radar observes precipitation in mid-latitudes (i.e. away from the nadir), the radar cannot observe weak precipitation at most of the altitude while it is easier to observe strong precipitation at any altitude.

6. Summary

We examined the feasibility of radar observation for precipitation from a geostationary satellite. The results demonstrated that it would be possible to obtain three-dimensional precipitation data. However, the quality of the observation was found to depend on the beam width, the beam sampling span, and the position of targeting precipitation systems. With the wide beam width and coarse beam span, the

345 radar cannot observe weak precipitation at low altitudes. The limitations can be somewhat mitigated
346 by oversampling (i.e., a wide beam width but a fine sampling span). With the narrow beam width and
347 fine beam sampling span, the surface clutter interference was confined to the surface level. For the
348 position of the target precipitation system, the larger (smaller) the off-nadir angle, the easier (more
349 difficult) it is to obtain the precipitation signal if the precipitation is strong (weak).

350 In this study, we did not consider attenuation, assuming that it can be corrected (e.g. Iguchi et al.,
351 2000). Also, we assumed that the area where SCR is greater than zero is observable, assuming that the
352 clutter filter would be available. Therefore, an attenuation correction method and a clutter filter should
353 be developed in the future. One possible idea for the filter may be to distinguish an echo from
354 precipitation and surface by using Doppler shift, but this remains to be a subject of future research.

355 If the wide beam width of 0.032° is used, the raw product may be prohibitively coarse for a specific
356 purpose. One possible way to effectively downscale such observations is to assimilate the data for
357 NWP. By doing this, the information can be treated properly, and we can get precipitation information
358 in the prediction model coordinate. However, it is not trivial whether assimilation of such data is useful
359 for NWP. In the future, an observing system simulation experiment (OSSE) will be conducted using
360 precipitation measurements simulated with the simulator developed in this study to evaluate the
361 potential impacts of the GeoSat/PR on NWP. Given that wind field observation may be possible from
362 a geostationary satellite as shown in Lewis et al. (2011), the combined use of both observations would
363 be an attractive option.

364

365 **Acknowledgement**

366 This study was partly supported by the Japan Aerospace Exploration Agency (JAXA); and the
367 FLAGSHIP2020 Project of the Ministry of Education, Culture, Sports, Science and Technology Japan.
368 The experiments were performed using the K computer at the RIKEN R-CCS (ra000015, hp160229,
369 hp170246, hp180194).

Atmos. Meas. Tech. Discuss., https://doi.org/10.5194/amt-2018-278
Manuscript under review for journal Atmos. Meas. Tech.
Discussion started: 9 November 2018

Atmospheric Measurement Techniques Discussions

372 **Reference**

373 Bessho, K., Date, K., Hayashi, M., Ikeda, A., Imai, T., Inoue, H., Kumagai, Y., Miyakawa, T., Murata,
374 H., Ohno, T., Okuyama, A., Oyama, R., Sasaki, Y., Shimazu, Y., Shimoji, K., Sumida, Y., Suzuki,
375 M., Taniguchi, H., Tsuchiyama, H., Uesawa, D., Yokota, H., Yoshida, An introduction to
376 Himawari-8/9: Japan's new-generation geostationary meteorological satellites, J. Meteorol. Soc.
377 JPN., 94, 151‐183, 2016.
378 Cho, H.-K., Bowman, P. B., and North, G. R., Equatorial waves including the Madden-Julian
379 Oscillation in TRMM rainfall and OLR data, J. Climate, 17, 4387-4406, 2004.
380 Gaspari, G., and Cohn, S., Construction of correlation functions in two and three dimensions, Q. J.
381 Roy. Meteor. Soc., 125, 723-757, 1999.
382 Hashino, T., Satoh, M., Hagihara, Y., Kubota, T., Matsui, T., Nasuno, T., and Okamoto, H., Evaluating
383 cloud microphysics from NICAM against CloudSat and CALIPSO, J. Geophys. Res. Atmos., 118,
384 7273-7292, 2013.
385 Hamada, A., Takayabu, Y. N., Liu, C., and Zipser, E. J., Weak linkage between the heaviest rainfall
386 and tallest storms, Nat. Commun, doi: 10.1038/ncomms7213, 2015.
387 Hou, A. Y., R. K. Kakar, S. Neeck, A. A. Azarbarzin, C. D. Kummerow, M. Kojima, R. Oki, K.
388 Nakamura, and T. Iguchi, 2014: The global precipitation measurement mission. Bull. Amer.
389 Meteor. Soc., 95, 701-722.
390 Houze, R. A., Rasmussen, K. L., Zuluaga, M. D., and Brodzik, S. R., The variable nature of convection
391 in the tropics and subtropics: A legacy of 16 years of the Tropical Rainfall Measuring Mission
392 satellite, Rev. Geophys., 53, 994-1021, 2015.
393 Iguchi, T., Kozu, T., Meneghini, R., Awaka, J., Okamoto, K., Rain-profiling algorithm for the TRMM
394 precipitation radar, J. Appl. Meteorol., 39, 2038-2052, 2000.
395 Im, E., Smith, E. A., Chandrasekar, V. C., Chen, S., Holland, G., Kakar, R., Tanelli, S., Marks, F., and
396 Tripoli, G., Workshop report on NEXRAD-In-Space -A geostationary satellite doppler weather
397 radar for hurricane studies, 33rd Conf. on Radar Meteorology, Cairns, QLD, Australia, Amer.
398 Meteor. Soc., 4B.5, 2007 [Available online at http://ams.confex.com/ams/pdfpapers/123726.pdf.].
399 Kelley, O. A., Stout, J., and Halverson, J. B., Tall precipitation cells in tropical cyclone eyewalls are
400 associated with tropical cyclone intensification, Geophys. Res. Lett., 31, L24112, 2004.
401 Kidd, C., Becker, A., Huffman, G. J., Muller, C. L. Joe, P., Skofronick-Jackson, G., and Kirschbaum,
402 D. B., So, how much of the earth's surface is covered by rain gauges?, B. Am. Meteorol, Soc.,
403 doi: 10.1175/BAMS-D-14-00283.1, 2016.
404 Kozu, T, T. Kawanishi, H. Kuroiwa, M. Kojima, K. Oikawa, H. Kumagai, K. Okamoto, M. Okumura,
405 H. Nakatshka, and K. Nishikawa, Development of precipitation radar onboard the Tropical
406 Rainfall Measuring Mission (TRMM) satellite. IEEE Trans. Geosci. Remote Sens., 39, 102-116,
407 2001.
408 Kummerow, C., W. Barnes, T. Kozu, J. Shiue, and J. Simpson, The Tropical Rainfall Measuring
409 Mission (TRMM) sensor package, J. Atmos. Oceanic Technol., 15, 808–-816, 1998.

410 Lewis, W. E., Im, E., Tanelli, S., Haddad, Z., Tripoli, G. J., Smith, E. A., Geostationary doppler radar
411 and tropical cyclone surveillance, J. Atmos. Ocean. Tech., 28, 1185-1191, 2011.
412 Li, X., He, J., Wang, C., Tang, S., Hou, X., Evaluation of surface clutter for future geostationary
413 spaceborne weather radar, Atmosphere, 8, 14, doi: 10.3390/atmos8010014, 2017.
414 Kubota, T., Shige, S., Hashizume, H., Aonashi, K., Takahashi, N., Seto, S., Hirose, M., Takayabu, Y.
415 N., Ushio, T., Nakagawa, K., Iwanami, K., Kachi, M., Okamoto, K., Global precipitation map
416 using satellige-borne microwave radiometers by the GSMaP Project: Production and validation,
417 IEEE T. Geosci. Remote., 45, 7, 2259-2275, 2007.
418 Masunaga, H., and Kummerow, C., Combined radar and radiometer analysis of precipitation profiles
419 for a parametric retrieval algorithm, J. Atmos. Ocean. Tech., 22, 909-929, 2005.
420 Morita, J., Takayabu, Y. N., Shige, S., Kodama, Y., Analysis of rainfall characteristics of the Madden-
421 Julian oscillation using TRMM satellite data, Dynam. Atmos. Oceans, 42, 207-126, 2006.
422 Nakanishi, M., and Niino, H., An improved Mellor–Yamada level-3 model with condensation physics:
423 Its design and verification, Bound.-Lay. Meteorol., 112, 1–31, 2004.
424 Okamoto, K., Aonashi, K., Kubota, T., Tashima, T., Experimental assimilation of the GPC Core
425 Observatory DPR reflectivity profiles for Typhoon Halong (2014), Mon. Weather Rev., 144,
426 2307-2326, 2016.
427 Otsuka, S., Kotsuki, S., Miyoshi, T., Nowcasting with data assimilation: A case of global satellite
428 mapping of precipitation, Weather Forecast., 31, 1409-1416, 2016.
429 Sekiguchi, M., and Nakajima, T., A k-distribution-based radiation code and its computational
430 optimization for an atmospheric general circulation model, J. Quant. Spectrosc. Ra.,J. Quant.
431 Spectrosc. Radiat. Transfer, 109, 2779–2793, 2008.
432 Skofronick-Jackson, G., Petersen, W. A., Berg, W., Kidd, C., Stocker, E. F., Kirschbaum, D. B., Kakar,
433 R., Braun, S. A., Huffman, G. J., Iguchi, T., Kirstetter, P. E., Kummerow, C., Meneghini, R., Oki,
434 R., Olson, W. S., Takayabu, Y., Furukawa, K., Wilheit, T., The global precipitation measurement
435 (GPM) mission for science and society, B. Am. Meteorol. Soc., 98, 1679-1695, 2017.
436 Takahashi, N., Surface echo characteristics derived from the wide swath experiment of the
437 precipitation radar onboard TRMM satellite during its end-of-mission operation, IEEE T. Geosci.
438 Remote., 55, 4, 1988-1993, 2017.
439 Takayabu, Y. N., Rain-yield per flash calculated from TRMM PR and LIS data and its relationship to
440 the contribution of tall convective rain, Geophys. Res. Lett., 33, L18705, 2006.
441 Tomita, H., New microphysical schemes with five and six categories by diagnostic generation of cloud
442 ice, J. Meteorol. Soc. JPN., 86A, 121-142, 2008.
443 Wentz, F. J., Peteherych, S., Thomas, L. A., A model function for ocean radar cross sections at 14.6
444 GHz, J. Geophys. Res., 89, c3, 3689-3704, 1984.
445

Atmos. Meas. Tech. Discuss., https://doi.org/10.5194/amt-2018-278
Manuscript under review for journal Atmos. Meas. Tech.
Discussion started: 9 November 2018

Atmospheric Measurement Techniques Discussions

446 **Tables**

447

448 **Table 1** Specifications of the precipitation radar aboard geostationary satellite

Parameter	Value
Frequency	13.6GHz
Scan angle	±6°
Range resolution	≤500m
Horizontal resolution	20km at nadir
Observation range	30km at nadir

449

450 **Table 2** Radar settings. The figures show the resolution at the nadir point.

Experiment	Beam width	Beam span
bw05bs05	5km	5km
bw20bs05	20km	5km
bw20bs20	20km	20km

451

452

Atmos. Meas. Tech. Discuss., https://doi.org/10.5194/amt-2018-278
Manuscript under review for journal Atmos. Meas. Tech.
Discussion started: 9 November 2018

Atmospheric Measurement Techniques Discussions

453 **Figures**

454

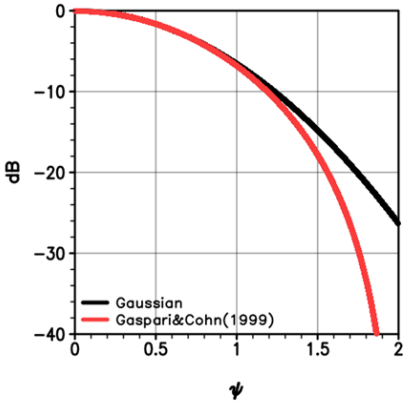

455

456 **Figure 1** Beam pattern (dB) as a function of normalized beam direction angle. Black and red curves
457 show the Gaussian function and the fitted fifth-order polynomial (Gaspari and Cohn, 1999),
458 respectively.

459

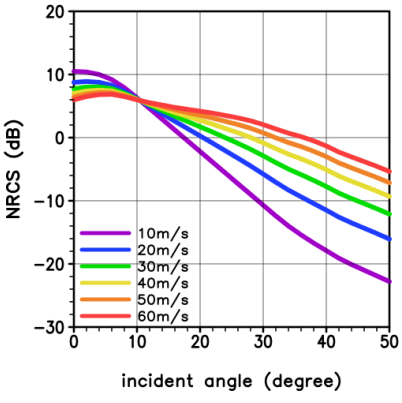

460

461 **Figure 2** Normalized radar cross section (dB) as a function of incident angle for six cases of 10-m
462 wind speed.

463

Atmos. Meas. Tech. Discuss., https://doi.org/10.5194/amt-2018-278
Manuscript under review for journal Atmos. Meas. Tech.
Discussion started: 9 November 2018

Atmospheric Measurement Techniques Discussions

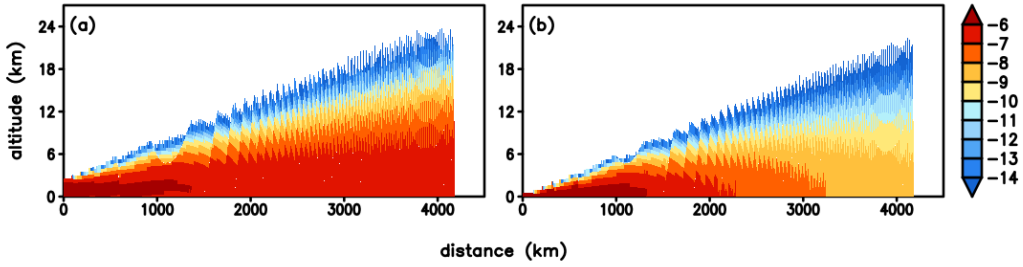

464
465 **Figure 3** Received power from (a) precipitation, and (b) sea surface clutter, normalized by $\mathbf{P_t}$ (dB).
466

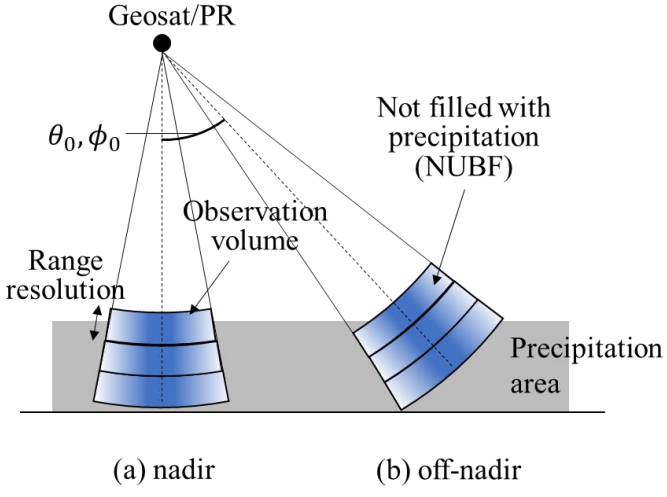

467
468 **Figure 4** Schematic image of the scattering volume at (a) nadir, and (b) off-nadir.
469

Atmos. Meas. Tech. Discuss., https://doi.org/10.5194/amt-2018-278
Manuscript under review for journal Atmos. Meas. Tech.
Discussion started: 9 November 2018

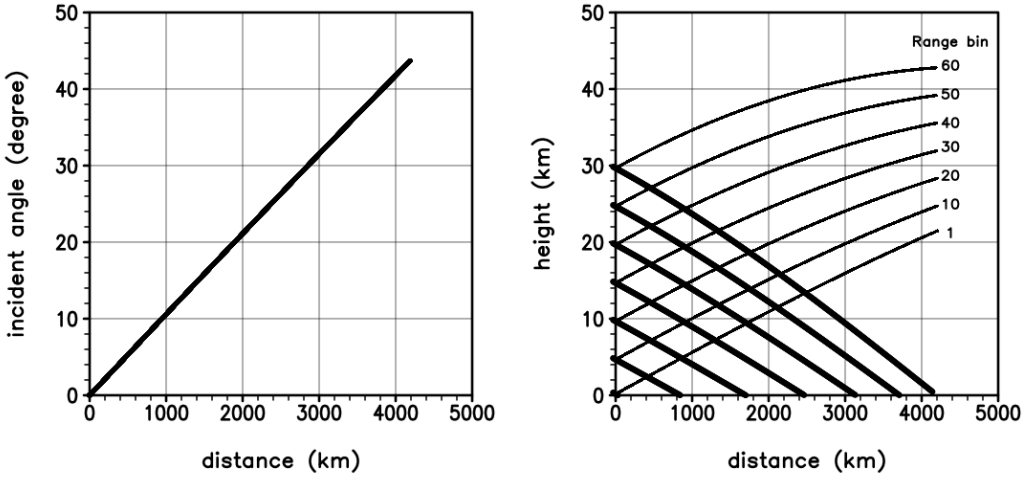

470

471 **Figure 5** Incident angle (a) and height of the radar scattering volume (b) as a function of the distance
472 from the nadir. Thick and thin lines in (b) shows the lower and upper bound, respectively.

473

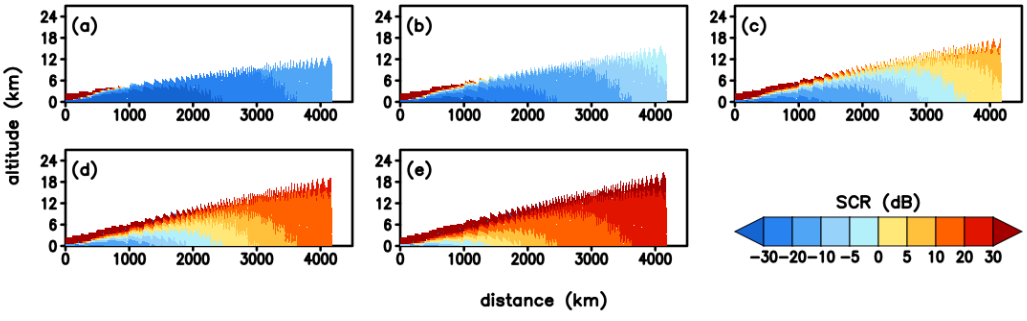

474

475 **Figure 6** Signal-to-clutter ratio (SCR) in measuring five precipitation intensity (a) 20, (b) 30, (c) 40,
476 (d) 50, and (e) 60 dBZ. It is assumed that the altitude lower than 2 km is filled with homogeneous
477 precipitation.

478

Atmos. Meas. Tech. Discuss., https://doi.org/10.5194/amt-2018-278
Manuscript under review for journal Atmos. Meas. Tech.
Discussion started: 9 November 2018

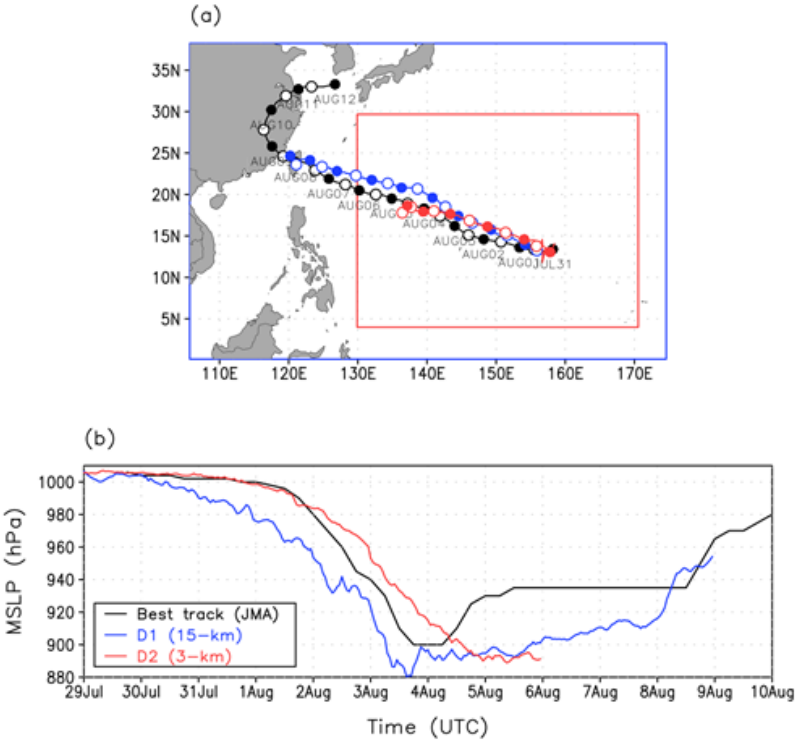

Figure 7 (a) Model domains for D1 (blue) and D2 (red) and typhoon tracks, and (b) time series of minimum sea level pressure (MSLP). Black, blue, and red colors show the JMA best track data, D1 simulation, and D2 simulation, respectively. Closed and open circles in (a) denote the typhoon positions at 0000 UTC and 1200 UTC, respectively.

Atmos. Meas. Tech. Discuss., https://doi.org/10.5194/amt-2018-278
Manuscript under review for journal Atmos. Meas. Tech.
Discussion started: 9 November 2018

Atmospheric Measurement Techniques Discussions

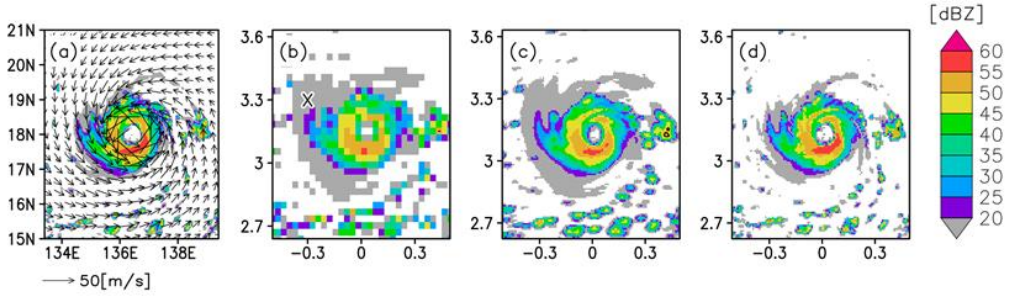

485

486 **Figure 8** Radar reflectivity (dBZ) near the surface in the typhoon mature stage (0000 UTC, 5 August
487 2015) for (a) the truth, (b) bw20bs20, (c) bw20bs05, and (d) bw05bs05. 10-m wind speed is overlaid
488 in (a). Note that the areas where reflectivity form precipitation larger than 0 dBZ are shaded.

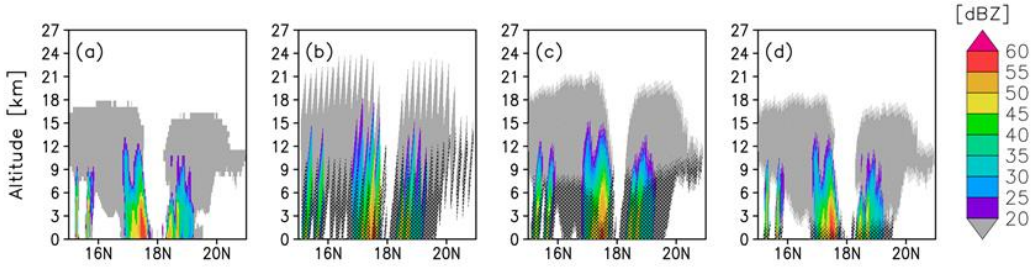

489

490 **Figure 9** Precipitation reflectivity (dBZ) along 136.4°E longitude line passing through the typhoon
491 center in the mature stage (0000 UTC, 5 August 2015) for (a) the truth, (b) bw20bs20, (c) bw20bs05,
492 and (d) bw05bs05. The area in which SCR < 0 is hatched in (b-d). Note that the areas where reflectivity
493 form precipitation larger than 0 dBZ are shaded.

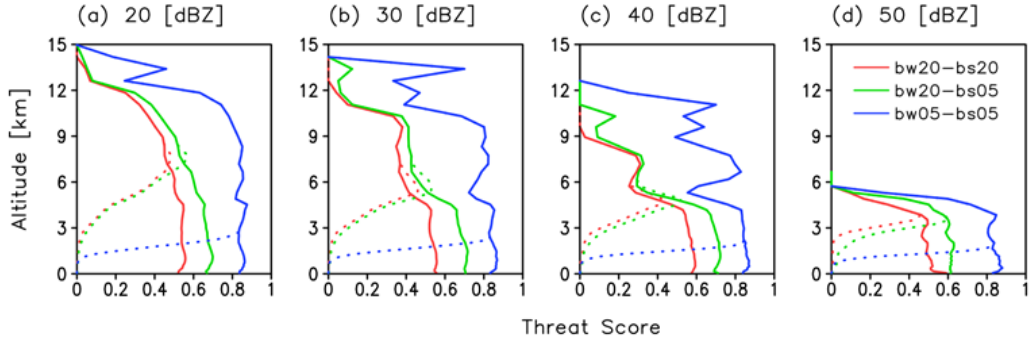

494

495 **Figure 10** Threat score with a threshold of (a) 20, (b) 30, (c) 40, and (d) 50 (dBZ) for bw20bs20 (red),
496 bw20bs05 (green), and bw05bs05 (blue). The dotted and solid lines show the threat score with and

Atmos. Meas. Tech. Discuss., https://doi.org/10.5194/amt-2018-278
Manuscript under review for journal Atmos. Meas. Tech.
Discussion started: 9 November 2018

Atmospheric Measurement Techniques Discussions

497 without considering the impact of surface clutter, respectively.

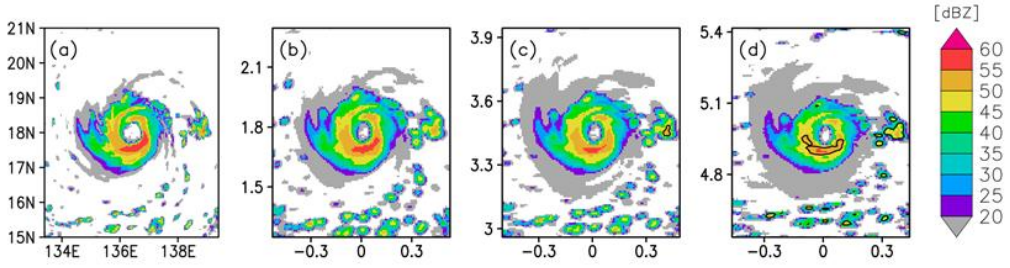

498

499 **Figure 11** Precipitation reflectivity (dBZ) measured with bw20bs05 for the typhoons whose center is
500 in (b) 10°N, (c) 20°N, and (d) 30°N. Contour in (b-d) corresponds to the area SCR > 0. Panel (a) shows
501 the truth. Note that the areas where reflectivity form precipitation larger than 0 dBZ are shaded.

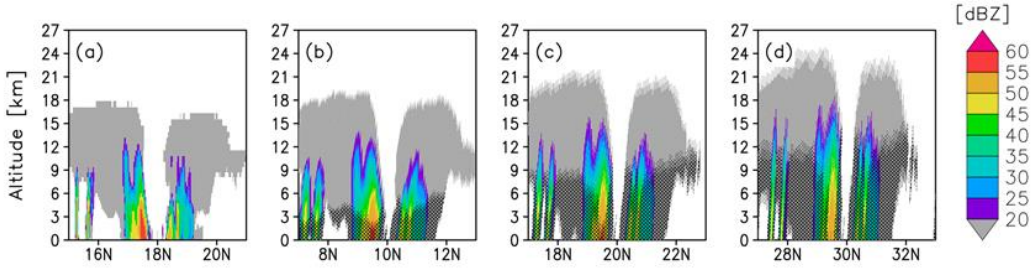

502

503 **Figure 12** Precipitation reflectivity (dBZ) along 136.4°E longitude line passing through the typhoon
504 center measured with bw20bs05 for the typhoons whose center is in (b) 10°N, (c) 20°N, and (d) 30°N.
505 The area in which SCR < 0 is hatched in (b-d). Panel (a) shows the truth. Note that the areas where
506 reflectivity form precipitation larger than 0 dBZ are shaded.

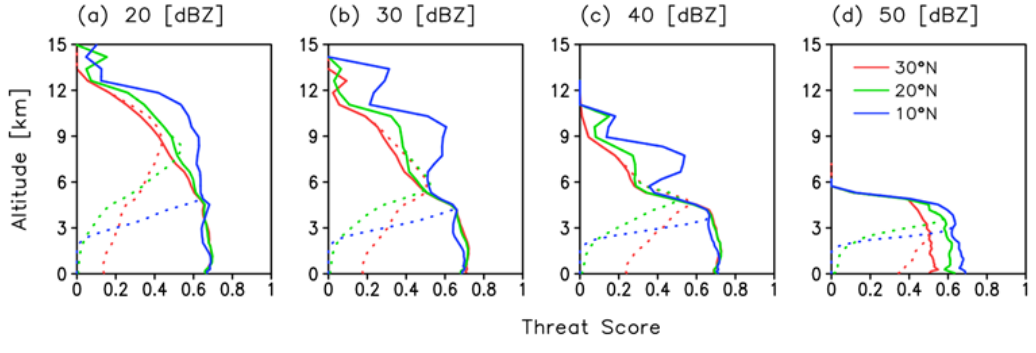

507

508 **Figure 13** Threat score with a threshold of (a) 20, (b) 30, (c) 40, and (d) 50 (dBZ) for the typhoons

Atmos. Meas. Tech. Discuss., https://doi.org/10.5194/amt-2018-278
Manuscript under review for journal Atmos. Meas. Tech.
Discussion started: 9 November 2018

Atmospheric Measurement Techniques Discussions

509 whose centers are at 30°N (red), 20°N (green), and 10°N (blue). The dotted and solid lines show the
510 threat score with and without considering the impact of surface clutter, respectively.

511

512